Single-Step Synthesis of Al-Doped TiO_2 Nanoparticles Using Non-Transferred Thermal Plasma Torch

2012 Jpn. J. Appl. Phys. 51 01AL01

(http://iopscience.iop.org/1347-4065/51/1S/01AL01)

Japanese Journal of Applied Physics **51** (2012) 01AL01 **REGULAR PAPER**
DOI: 10.1143/JJAP.51.01AL01

Single-Step Synthesis of Al-Doped TiO_2 Nanoparticles Using Non-Transferred Thermal Plasma Torch

Cheng-Yen Tsai, Hsing-Cheng Hsi[1]*, Hsunling Bai[2], Kuo-Shuh Fan[3], and Hung-Dar Sun[3]

Graduate Institute of Engineering Science and Technology, National Kaohsiung First University of Science and Technology, Kaohsiung 811, Taiwan
[1]*Institute of Environmental Engineering and Management, National Taipei University of Technology, Taipei 106, Taiwan*
[2]*Institute of Environmental Engineering, National Chiao Tung University, Hsinchu 300, Taiwan*
[3]*Department of Safety, Health and Environmental Engineering, National Kaohsiung First University of Science and Technology, Kaohsiung 811, Taiwan*

Received March 31, 2011; accepted September 22, 2011; published online January 20, 2012

Al-doped TiO_2 nanoparticles possessing visible-light photocatalytic activity were fabricated with an atmospheric-pressure thermal plasma system via a single-step direct combination of vaporized Ti, Al, and O_2. Pure Ti and Al_2O_3 powders and ultrahigh-purity O_2 were used as the precursors. The experimental results showed that the size of synthesized TiO_2 was between 10 and 105 nm. Nevertheless, the nanoparticles with sizes smaller than 50 nm accounted for approximately 80% of the total number. The observed size reduction appeared to be the suppression on particle growth due to the introduction of Al species into TiO_2 crystal. The largest specific surface area of the Al-doped TiO_2 was 44 $m^2 \cdot g^{-1}$. The anatase phase was noticeably decreased with increasing the Al_2O_3 addition. The absorption spectra of Al-doped TiO_2 shifted from UV to visible-light region with respect to an increase in Al_2O_3 addition. Oxygen in the formed TiO_2 was found to be in TiO_2 crystal lattice and in surface hydroxyl groups. Both Ti^{4+} and Ti^{3+} existed in the formed TiO_2. However, the Ti^{3+} amount significantly increased with increasing Al_2O_3 addition due to Al/Ti substitution and the resulted oxygen vacancy.

1. Introduction

Titanium dioxide (TiO_2) has been extensively studied due to its photocatalytic effects and potentials in industrial applications. TiO_2 is also known to effectively decompose various pollutants in gaseous and aqueous phases. The fabricating processes strongly affect the purity and surface properties of resulting TiO_2 nanoparticles, which subsequently influence the photocatalytic characteristics. Several liquid- or vapor-phase syntheses have been proposed to prepare TiO_2 nanoparticles and nanofilms, such as sol–gel methods,[1–3] thermal hydrolysis,[4] hydrothermal processing,[5] chemical vapor deposition,[6] and thermal plasma approaches.[7–10] Sol–gel methods have been widely used in bench-scale nanoparticle production due to its simplicity to operate. However, the concentration of reagents, reaction time, solution pH, and temperature strongly affect the growth of TiO_2 photocatalyst. Additionally, because the processing temperature of sol–gel methods is relatively low (i.e., around 373 K), subsequent calcination is needed to transform the obtained TiO_2 into anatase, which has been characterized as the most effective phase for photocatalytic application.

Thermal plasma has been shown to possess advantages to develop nanoparticles with clean surface and narrow particle size distribution. The sufficient energy provided by thermal plasma can directly vaporize liquid and solid precursors and induce the TiO_2 formation. $TiCl_4$(aq) is frequently used as the TiO_2 precursor.[7,11,12] However, Cl_2 generated from the thermal plasma process arouses environmental concerns. Theoretically, TiO_2 nanoparticles with high purity can be developed via a direct combination of Ti and O atom. Nevertheless, Ti metal has a high melting point at 1941 K that makes the direct combination difficult to occur. Using thermal plasma as heating source can successfully vaporize Ti metal and make the direct combination process feasible.[13]

TiO_2 photocatalyst has a large energy band gap (3.2 eV for anatase and 3.0 eV for rutile) causing the photocatalytic reactions only occurring under UV irradiation. Visible-light TiO_2 photocatalysts have thus drawn great attention in recent years. Doping TiO_2 photocatalysts with metal ions can improve the photocatalytic activity of TiO_2 under visible light because the impurity energy levels in the band gap are formed and result in alteration of electron hole recombination.[14] Doping metals into TiO_2 can also be achieved with thermal plasma. A study showed that metals such as Fe, Al, V, Nb, Sb, and Sn can be successfully doped into TiO_2 using thermal plasma.[15] Oh *et al.* prepared pure TiO_2, Si-doped TiO_2, and Fe-doped TiO_2 from $TiCl_4$, $SiCl_4$, and $(CH_3COCHCOCH_3)_3Fe$ with thermal plasma.[16] Li *et al.* synthesized Er-doped TiO_2 by thermal plasma oxidation of a liquid precursor containing titanium butoxide and erbium nitrate.[17] Wang *et al.* fabricated Fe-doped TiO_2 ultrafine powders using induction thermal plasma.[18] The most important influences of dopant addition on TiO_2 are enhancing reactivity under visible light, a reduction in grain growth, and an increase in conductivity.

Because the ionic radii for Al and Ti are close (0.061 nm for Ti^{4+} and 0.053 nm for Al^{3+}), Al can successfully fill into a regular cation position and create a substitutional solid solution. Moreover, Al-doped TiO_2 and ZnO ceramics were shown to have higher sensitivity to humidity in thick and thin films,[19,20] making Al-doped TiO_2 a great candidate as gas sensors in application. Several works have shown that Al-doped TiO_2 nanoparticles can be fabricated via liquid-phase[14,21–25] or vapor-phase syntheses.[6,12,26] $TiCl_4$, $Ti(OC_4H_9)_4$, $Ti(OC_3H_7)_4$, $Al[OCH(CH_3)_2]_3$, $Al_2(SO_4)_3$, $Al(NO_3)_3$, $AlCl_3$, and Al_2O_3 can be used as precursors. Lee *et al.* prepared Al-doped TiO_2 using thermal plasma. $TiCl_4$ and $AlCl_3$ were fed into the DC plasma jet. The authors concluded that doped Al species inhibited the particle growth and the absorption band of synthesized powers shifted from the UV region to the visible-light region.[12] Choi *et al.* synthesized Al-doped TiO_2 nanopowders for gas sensors using a citrate-nitrate auto combustion

*E-mail address: hchsi@ntut.edu.tw

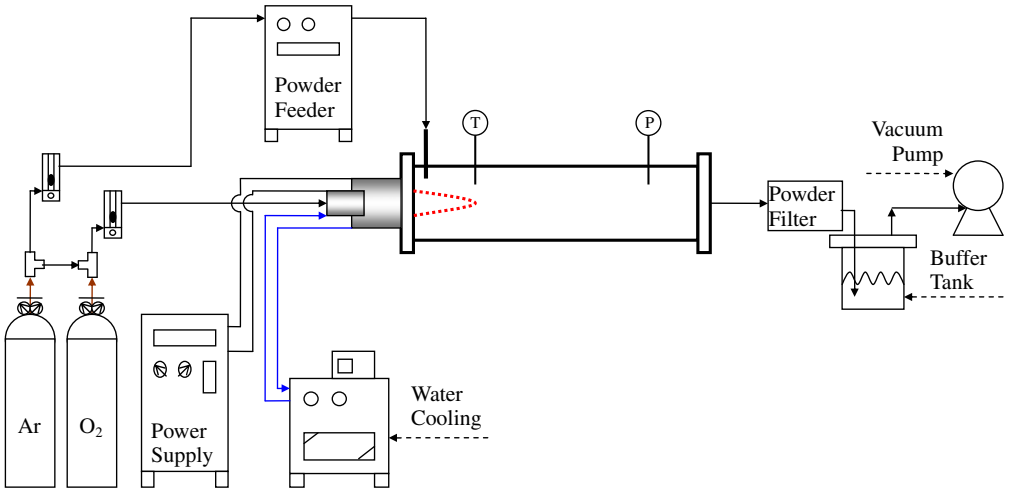

Fig. 1. (Color online) Thermal plasma apparatus for fabricating Al-doped TiO_2 nanoparticles.

method with Ti solution and $Al(NO_3)_3$ solution. The authors reported that Al-doped TiO_2 gas sensors were more selective and sensitive to CO and O_2 at an operating temperature of 600 °C than pure TiO_2 powders.[25)]

Notably, few studies focused on producing Al-doped TiO_2 nanoparticles from pure Ti metal. In our previous study, high-purity TiO_2 nanoparticles using Ti metal as a precursor were successfully fabricated with a transferred plasma torch.[27)] In the present work, Al-doped TiO_2 nanoparticles were prepared in a single-step process (i.e., without subsequent calcination and surface reduction) using an atmospheric-pressure non-transferred thermal plasma system. Pure Ti and Al_2O_3 powders and ultrahigh-purity O_2 were chosen as the precursors not only because they are easily delivered into the reaction chamber but also due to their high purity (i.e., without Cl or S). The aim is at directly combining vaporized Ti, Al, and O atoms under the high-temperature plasma flame to form Al-doped TiO_2 nanoparticles possessing visible-light photocatalytic activity. It was expected that the thermal plasma can offer sufficient energy to dope Al into the crystal of TiO_2 and cause substitution of Ti instead of physically depositing the Al_2O_3 onto the TiO_2 surface.

2. Experimental Procedure

2.1 Preparation of Al-doped TiO_2 nanoparticles

Al-doped TiO_2 nanoparticles were synthesized from pure Ti powder (99.8%), Al_2O_3 powder (99.9%), and ultrahigh-purity (UHP) O_2 in an atmospheric-pressure thermal plasma reactor (Fig. 1). The system mainly comprises a stainless steel chamber (SS310 with inner diameter = 30 cm and length = 100 cm), a DC non-transferred plasma torch, a DC power supply (Taiwan Plasma PHS-15C), a stainless steel powder feeder, a powder filter, a vacuum pump (ULVAC GVD-050A), and a buffer tank for capturing the particles which bypassed filter floating in the exhaust gas. The torch electrode made of copper alloy was water-cooled. The system was operated at 40 A and 200 V. UHP Ar and O_2 were mixed as the plasma gas with a flow rate of 60 $L \cdot min^{-1}$ at $Ar : O_2 = 3 : 1$ by volume. The Ti and Al_2O_3 powder feedstock was vertically injected into the plasma system using 2 $L \cdot min^{-1}$ Ar as the carrier gas. The total powder feeding rate was fixed at 0.2 $g \cdot min^{-1}$. The Al_2O_3/Ti mass ratio was controlled at 0, 0.1, 0.2, and 0.4. The gas stream containing the synthesized TiO_2 nanoparticles passed through the powder filter in which the synthesized nanoparticles were collected.

2.2 Characterization of Al-doped TiO_2

The particle size of synthesized Al-doped TiO_2 nanoparticles were determined with a transmission electron microscope (TEM; Philips CM-200) by visually counting. The test sample was prepared on a copper mesh substrate covered with a carbon film for TEM analysis. Brunauer–Emmett–Teller (BET) specific surface area was analyzed using a Beckman Coulter SA3100 based on the N_2 adsorption isotherm obtained at 77 K. The phase compositions of nanoparticles were analyzed with an X-ray powder diffractometer (XRD; Rigaku Rinet 200) with Cu Kα radiation ($\lambda = 1.5405$ Å). The scan range (2θ) was from 20 to 80° with a scanning rate of 0.02° s^{-1}. The crystalline phases were identified with JCPDS database. The mass fractions of anatase to rutile in synthesized nanoparticles were then calculated using the following equation:[28)]

$$f_A = \frac{1}{1 + 1.26 I_R / I_A} \quad (1)$$

where f_A is the mass fraction of anatase, I_R is the intensity of (110) reflection of rutile, and I_A is the intensity of (101) reflection of anatase. The UV–visible diffuse reflection spectra ranging from 300 to 800 nm were acquired with a spectrophotometer (Hitachi U-3010). The composition and Ti, O, Al, and Cu bonding patterns were examined using an X-ray photoelectron spectroscope (XPS; ULVAC-PHI 1600). The obtained XPS spectra were deconvoluted with the XPSPEAK® software. All binding energies (BE) were referred to C 1s line at 285 eV.

3. Results and Discussion

The TEM images of Al-doped TiO_2 developed under various Al_2O_3/Ti mass ratios were shown in Fig. 2. TEM results revealed that the formed nanoparticles were homogenous, without significant phase separation or coating on the surface. The shape of the formed nanoparticles was in

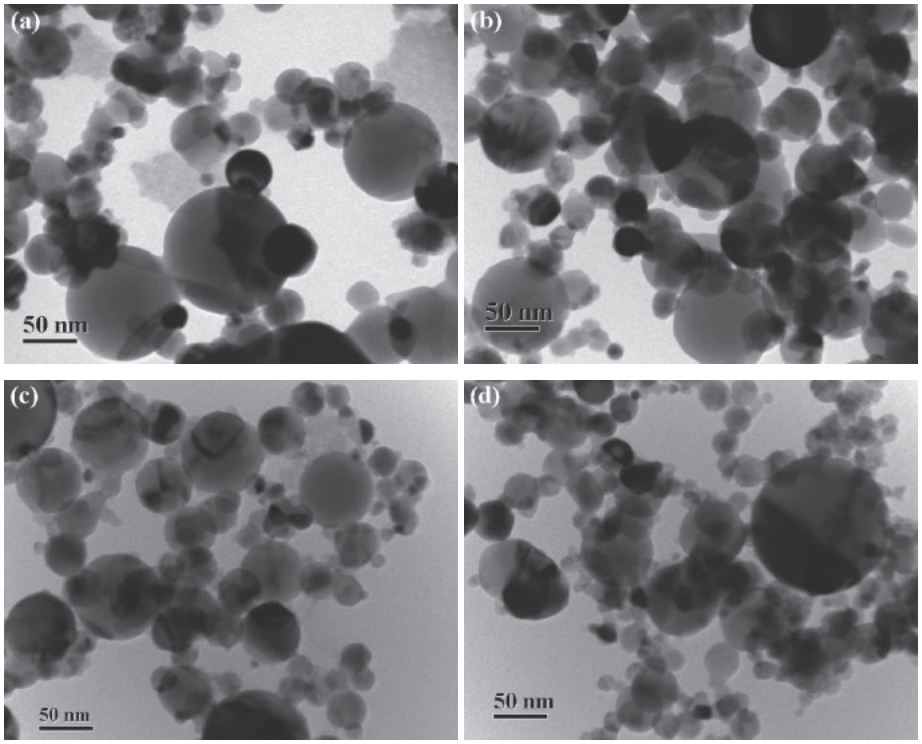

Fig. 2. TEM images of TiO_2 nanoparticles synthesized at Al_2O_3/Ti mass ratio of (a) 0, (b) 0.1, (c) 0.2, and (d) 0.4.

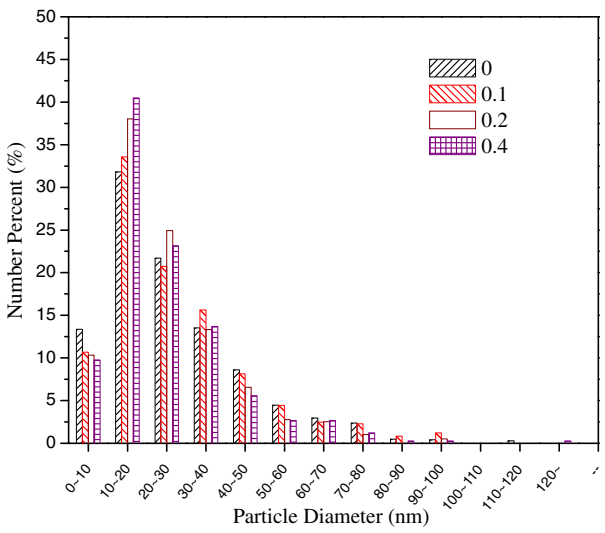

Fig. 3. (Color online) Particles size distributions of TiO_2 nanoparticles synthesized at $Al_2O_3/Ti = 0$, 0.1, 0.2, and 0.4.

general spherical. The nanoparticle size was approximately between 10 and 105 nm. It was noteworthy that the sizes of the feedstock Al_2O_3 and Ti powders were about 5–15 µm. These observations suggested that the injected Al_2O_3 and Ti powders vaporized and subsequently formed Al-doped TiO_2 nanoparticles in the thermal plasma environment via the recombination of vaporized Al, Ti, and O atoms. The particle size distributions of resulting TiO_2 estimated based on the TEM images are shown in Fig. 3. Particles having size between 10 and 20 nm accounted for 32–43% of the total number, followed by those with size between 20 and 30 nm accounting for 18–25%. Additionally, the nanoparticles with size smaller than 50 nm accounted for 89–93% and those with size large than 70 nm were <5% indicating the success of using thermal plasma torch to fabricate TiO_2 particles in nanoscale. Notably, the amount of nanoparticles with size within 10–20 nm slightly increased as increasing the Al_2O_3/Ti mass ratio. The observed size reduction may be attributed to the suppression of particle growth by the introduction of Al species into TiO_2 crystal. It has been shown that in the anatase or rutile crystal structure, most of the doped Al^{3+} ions occupied substitutional sites rather than the interstitial sites.[29] Substitutional defects may cause a slight decrease in the metal–oxygen bond distances due to the smaller ionic radius of Al^{3+} compared to that of Ti^{4+}, which could induce local crystal frustration; consequently, the Al-doped TiO_2 crystal structure could be distorted and the particle nucleation and growth of TiO_2 were inhibited or suppressed. De Villeneuve *et al.* reported that impurities influence the nucleation, growth, and structure of crystals. The growth rate sensitively depends on the impurity's size. Crystal growth is inhibited to a greater extent near smaller impurities, pointing to local crystal frustration induced by the curvature of the impurity.[30] Kubota also addressed that the crystal growth is markedly affected by impurities present in the system.[31] Our observational results are also in agreement with several previous studies.[12,26,32]

The BET surface area of synthesized nanoparticles was calculated based on the N_2 adsorption isotherms obtained at 77 K. The surface areas for samples prepared at the Al_2O_3/Ti mass ratios of 0, 0.1, 0.2, and 0.4 were 41.0, 40.4, 44.1, and 37.6 $m^2 \cdot g^{-1}$, respectively, indicating that the surface area of Al-doped TiO_2 was less affected by the amount of Al doping and mainly determined by the size of the samples.

Figure 4 shows the XRD powder patterns for the nanoparticles synthesized at various Al_2O_3/Ti mass ratios. All the resulting TiO_2 nanoparticles possessed both anatase

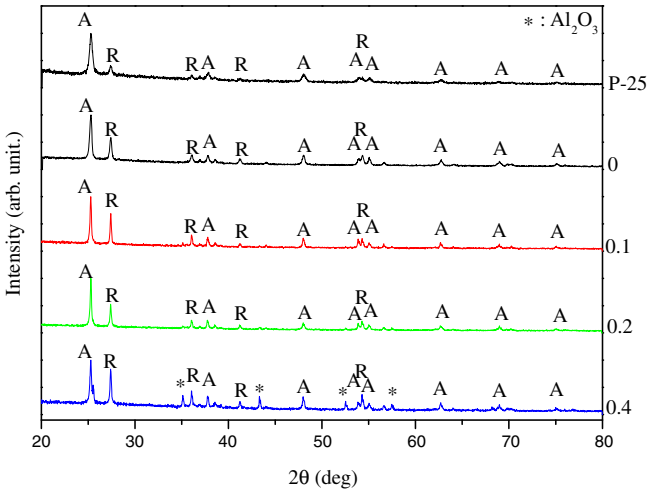

Fig. 4. (Color online) XRD patterns of commercial P-25 TiO_2 and TiO_2 nanoparticles synthesized at $Al_2O_3/Ti = 0$ to 0.4.

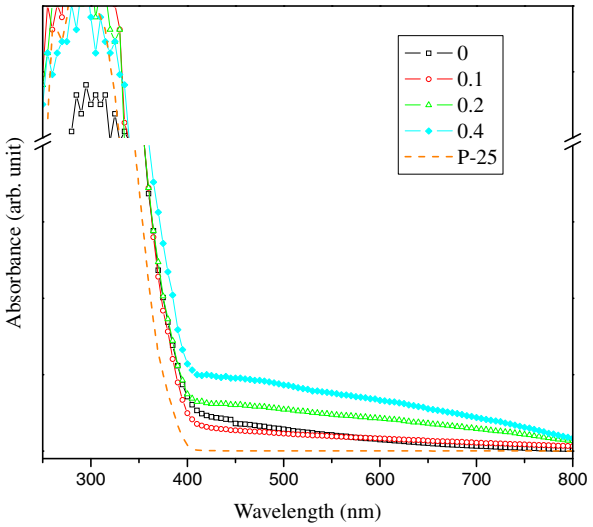

Fig. 5. (Color online) UV–visible absorption spectra of synthesized TiO_2 nanoparticles and P-25 TiO_2.

Table I. Crystal phases of Al-doped TiO_2 synthesized at various Al_2O_3/Ti mass ratio.

Al_2O_3/Ti mass ratio	f_A (wt%)	Phase detected
0	58.2	Anatase, rutile
0.1	56.4	Anatase, rutile
0.2	55.9	Anatase, rutile
0.4	51.1	Anatase, rutile, Al_2O_3

Table II. Atomic percentage of synthesized TiO_2 nanoparticles based on XPS examinations.

Al_2O_3/Ti mass ratio	Composition (at.%)			
	O	Al	Cu	Ti
0	72.34	0	2.94	24.72
0.1	67.52	5.20	3.31	23.96
0.2	62.73	13.85	3.26	19.94
0.4	60.48	19.66	3.61	16.26

and rutile crystalline phases. XRD results also showed that the diffraction peaks standing for Al_2O_3 appeared as $Al_2O_3/Ti = 0.4$, based on $2\theta = 35.15$, 43.35, 52.5, and 57.5° that are indexed to the Al_2O_3 diffraction pattern. These analytical results suggested that at a high Al_2O_3 loading, the thermal plasma flame became less effective in turning the Al_2O_3 into vapor phase and promoting the interactions between Al, Ti, and O atoms. Furthermore, the relative content of anatase, represented using the f_A value (Table I), was noticeably decreased with increasing Al_2O_3/Ti due to transformation into rutile. It has been well known that the rutile content increased with elevating reaction temperature.[15] However, the TiO_2 synthesis was performed at a constant plasma power of 8 kW. As a consequence, the variation in plasma temperature during different test conditions (i.e., various Al_2O_3/Ti ratios) was small and may not account for the enhancing XRD peak intensity for rutile. Numerous studies have shown the enhancement in transformation of anatase to rutile with increasing Al doping.[12,24,26,32] The experimental results presented here echo those early findings.

The absorption edge of synthesized nanoparticles and commercial Degussa P-25 TiO_2 examined using a UV–visible spectrophotometer is illustrated in Fig. 5. As it was expected, the P-25 TiO_2 lacked significant absorption above the basic absorption sharp edge at 390–400 nm. However, synthesized TiO_2 possessed an estimated band gap absorption upward 400 nm, indicating that the red shift and broadening in the visible light absorption range occurred. The absorption spectra of Al-doped TiO_2 shifted from UV to visible region with respect to an increase in Al_2O_3 addition can be assigned to the band gap narrowing relation to the interstitial Al species in the TiO_2 crystal.[12,14,23] Notably, the non-Al-doped TiO_2 synthesized in the thermal plasma flame also showed band gap absorption upward 400 nm, which was comparable to that of Al-doped TiO_2 developed at $Al_2O_3/Ti = 0.1$ (Fig. 5). This band gap absorption red shift may be resulted from the oxygen vacancy in the non-Al-doped TiO_2 crystal formed in the high-temperature plasma flame. Nakamura *et al.* suggested that the appearance of the visible light activity was attributed to the newly formed oxygen vacancy state between the valence and the conduction bands in the TiO_2 band structure.[33] This defect structure varies with the magnitude of oxygen vacancy, which depends on temperature, gas pressure, metal impurities, etc.[34]

The synthesized TiO_2 nanoparticles was examined using XPS to better understand the relative contents and bonding patterns of O, Al, Ti, and Cu. In generally, the contents (in at.%) of O and Ti decreased with increasing Al doping (Table II). The O_{1s} spectrum within 527–534 eV was successfully deconvoluted into two asymmetry peaks at 530.0 and 532.0 eV, indicating the presence of oxygen in the TiO_2 crystal lattice and in the surface hydroxyl groups (i.e., chemisorbed oxygen), respectively.[35,36] The Al 2p spectrum with a peak at around 75.5 eV confirmed the success of Al doping into the nanoparticle.

The Ti 2p XPS spectrum obtained from the Al-doped TiO_2 nanoparticles was deconvoluted into four peaks

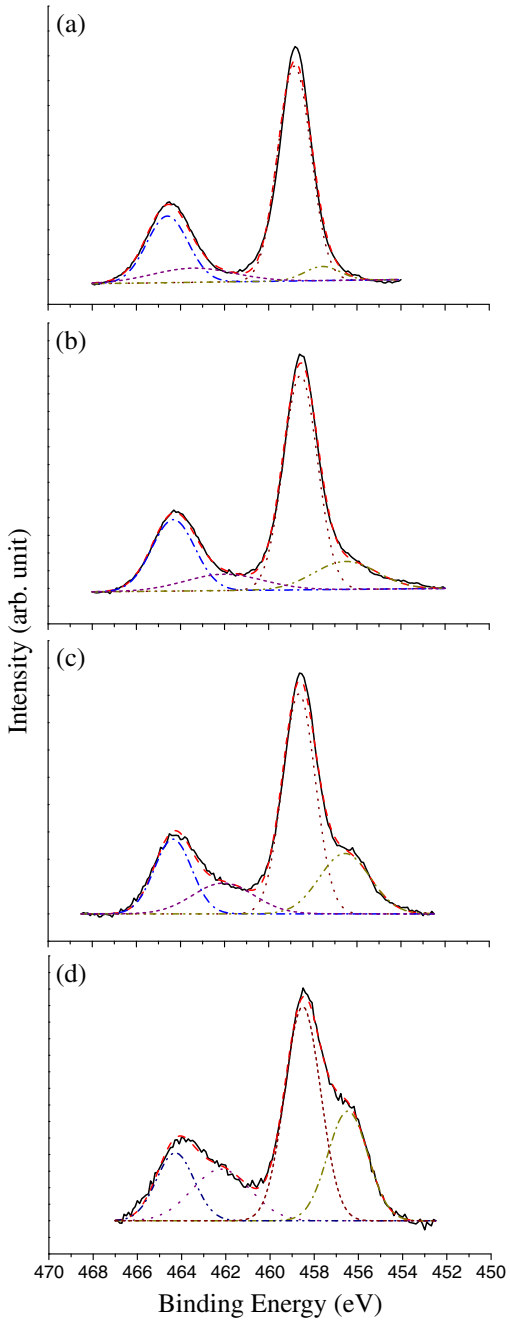

Fig. 6. (Color online) Ti 2p XPS spectra of TiO_2 synthesized at Al_2O_3/Ti mass ratio of (a) 0, (b) 0.1, (c) 0.2, and (d) 0.4.

within 456.4–464.4 eV, including Ti^{4+} $2p_{1/2}$, Ti^{3+} $2p_{1/2}$, Ti^{4+} $2p_{3/2}$, and Ti^{3+} $2p_{3/2}$ (Fig. 6). These peaks are indications to the presence of TiO_2 (Ti^{4+} $2p_{1/2}$ and Ti^{4+} $2p_{3/2}$) and Ti_2O_3 (Ti^{3+} $2p_{1/2}$ and Ti^{3+} $2p_{3/2}$), respectively.[37] The calculated $Ti^{3+}/(Ti^{3+} + Ti^{4+})$ ratios for samples produced at $Al_2O_3/Ti = 0$, 0.1, 0.2, and 0.4 were 2.6, 13.3, 27.9, and 41.9%, respectively, based on the deconvoluted peak area. These results suggested that Ti^{3+} content significantly increased with increasing Al_2O_3 addition due to transformation of TiO_2 into Ti_2O_3. Isomorphous substitution of Ti^{4+} with Al^{3+} appears to occur during the Al doping. The ionic radii of Al^{3+}, Ti^{4+}, and Ti^{3+}, however, are 0.053, 0.061, and 0.067 nm, respectively. When Al^{3+} dopants substitute Ti^{4+} from TiO_2 crystal, the lattice mismatch occurs due to the fact that the ionic radius of Al^{3+} is smaller than that of Ti^{4+}. To compensate for the smaller ionic radius of Al^{3+}, a species with an ionic radius larger than that of Ti^{4+} is needed. Apparently, Ti^{3+} is such a candidate. The same observation has been reported by Steveson *et al.*[38] In addition, the formal charge produced by the substitution of Ti^{4+} with Al^{3+} can also be compensated via the formation of O^- from O^{2-} and lead to the oxygen vacancies observed in Al-doped TiO_2.[21,26,38]

It is important to note that approximately 2.9–3.6 at. % Cu was observed in the synthesized TiO_2 based on the XPS examination (Table II). The Cu impurity was suspected to come from the plasma torch made of Cu alloy. Namely, in the high-temperature plasma environment, the plasma torch released Cu in vapor phase and subsequently impregnated into the TiO_2 nanoparticles. Accompanying the aforementioned results from the UV–visible examination, the doped Cu associated with the oxygen vacancy in non-Al-doped TiO_2 may synergistically contribute to the observed red shift in the UV–visible absorption spectrum. Zhang *et al.* reported that Cu with concentration smaller than 38 at. % in TiO_2 had insignificant effects on the Ti_{2p} binding energy.[39] Consequently, the increase in Ti^{3+} should be mainly resulted from the Al doping into TiO_2 crystal. The extent of red shift in the absorption spectra of nanoparticles thus mainly corresponded to the amount of Al doping and the presence of oxygen vacancy (Fig. 5). The Cu-doping effects on visible light activity may be less significant compared to Al in this case, which remained to be further studied.

4. Conclusions

Al-doped TiO_2 nanoparticles with visible-light photocatalytic activity were successfully synthesized in a single step using Ti powders, Al_2O_3 powders, and O_2 as the precursors under an atmospheric-pressure non-transferred thermal plasma environment. The formed nanoparticles had particle sizes within 10 to 105 nm and the samples with sizes smaller than 50 nm accounted for approximately 80% of the total number. The BET surface area of the Al-doped TiO_2 nanoparticles was between 37 and 44 $m^2 \cdot g^{-1}$. All the synthesized Al-doped TiO_2 consisted of both anatase and rutile phases; nevertheless, the ratio of anatase to rutile decreased with increasing Al_2O_3 addition. The substitution of Ti^{4+} with Al^{3+} and oxygen vacancy in the TiO_2 crystal caused by the high temperature plasma flame may lead to the red shift in the absorption edge to lower energy due to band gap narrowing. The phase transformation from TiO_2 to Ti_2O_3 appeared to result from the Al doping into and oxygen vacancy in the TiO_2 crystal.

Acknowledgements

This work was supported by National Science Council of Taiwan (NSC95-2622-E-327-002-CC3) and Taiwan Plasma Corporation, Kaohsiung, Taiwan. The authors also acknowledge Mr. Chin-Cheng Ho, Taiwan Plasma Corporation for his technical assistance.

1) H. Yamashita, M. Harada, J. Misaka, M. Takeuchi, K. Ikeue, and M. Anpo: J. Photochem. Photobiol. A **148** (2002) 257.
2) S. Qiu and S. J. Kalita: Mater. Sci. Eng. A **435–436** (2006) 327.
3) M. Kanna and S. Wongnawa: Mater. Chem. Phys. **110** (2008) 166.

4) M. C. Hidalgo and D. Bahnemann: Appl. Catal. B **61** (2005) 259.
5) X. H. Xia, Y. Liang, Z. Wang, J. Fan, Y. S. Luo, and Z. J. Jia: Mater. Res. Bull. **43** (2008) 2187.
6) X. Zhang, M. Zhou, and L. Lei: Appl. Catal. A **282** (2005) 285.
7) S. M. Oh and D. W. Park: Thin Solid Films **386** (2001) 233.
8) Y. L. Li and T. Ishigaki: Thin Solid Films **407** (2002) 79.
9) I. Banerjee, S. Karmakar, N. V. Kulkarni, A. B. Nawale, V. L. Mathe, A. K. Das, and S. V. Bhoraskar: J. Nanopart. Res. **12** (2010) 581.
10) Y. Tanaka, T. Nagumo, H. Sakai, Y. Uesugi, Y. Sakai, and K. Nakamura: J. Phys. D **43** (2010) 265201.
11) Y. Gou, D. Chen, and Z. Su: Appl. Catal. A **261** (2004) 15.
12) J. E. Lee, S. M. Oh, and D. W. Park: Thin Solid Films **457** (2004) 230.
13) C. J. Liu, G. P. Vissokov, and B. W. L. Jang: Catal. Today **72** (2002) 173.
14) H. K. Shon, D. L. Cho, S. H. Na, J. B. Kim, H. J. Park, and J. H. Kim: J. Ind. Eng. Chem. **15** (2009) 476.
15) S. Karvinen: Solid State Sci. **5** (2003) 811.
16) S. M. Oh, S. S. Kim, J. E. Lee, T. Ishigaki, and D. W. Park: Thin Solid Films **435** (2003) 252.
17) J. G. Li, X. H. Wang, H. Kamiyama, T. Ishigaki, and T. Sekiguchi: Thin Solid Films **506–507** (2006) 292.
18) X. H. Wang, J. G. Li, H. Kamiyama, and T. Ishigaki: Thin Solid Films **506–507** (2006) 278.
19) W. P. Tai and J. H. Oh: J. Mater. Sci.: Mater. Electron. **13** (2002) 391.
20) W. P. Tai, J. G. Kim, and J. H. Oh: Sens. Actuators B **96** (2003) 477.
21) U. Gesenhues and T. Rentschler: J. Solid State Chem. **143** (1999) 210.
22) U. Gesenhues: J. Photochem. Photobiol. A **139** (2001) 243.
23) B. Y. Lee, S. H. Park, M. Kang, S. C. Lee, and S. J. Choung: Appl. Catal. A **253** (2003) 371.
24) M. Wang, B. Gong, X. Yao, Y. Wang, and R. N. Lamb: Thin Solid Films **515** (2006) 2055.
25) Y. J. Choi, Z. Seeley, A. Bandyopadhyay, S. Bose, and S. A. Akbar: Sens. Actuators B **124** (2007) 111.
26) C. Li, L. Shi, D. Xie, and H. Du: J. Non-Cryst. Solids **352** (2006) 4128.
27) C. Y. Tsai, H. C. Hsi, H. Bai, K. S. Fan, and C. Chen: J. Nanopart. Res. **13** (2011) 4739.
28) R. A. Spurr and H. Myers: Anal. Chem. **29** (1957) 760.
29) J. F. Stebbins, I. Farnan, and U. Klabunde: J. Am. Ceram. Soc. **72** (1989) 2198.
30) V. W. A. de Villeneuve, R. P. A. Dullens, D. G. A. L. Aarts, E. Groeneveld, J. H. Scherff, W. K. Kegel, and H. N. W. Lekkerkerker: Science **309** (2005) 1231.
31) N. Kubota: Cryst. Res. Technol. **36** (2001) 749.
32) M. L. Taylor, G. E. Morris, and R. St. C. Smart: J. Colloid Interface Sci. **262** (2003) 81.
33) I. Nakamura, N. Negishi, S. Kutsuna, T. Ihara, S. Sugihara, and K. Takeuchi: J. Mol. Catal. A **161** (2000) 205.
34) P. Kofstad: in *Nonstoichiometry, Diffusion, and Electrical Conductivity in Binary Metal Oxides* (Wiley, New York, 1972) Chap. 8.
35) G. B. Song, H. Joly, F. S. Liu, T. J. Peng, P. Wan, and J. K. Liang: Appl. Surf. Sci. **220** (2003) 159.
36) L. Jing, X. Sun, W. Cai, Z. Xu, Y. Du, and H. Fu: J. Phys. Chem. Solids **64** (2003) 615.
37) C. T. Wang and S. H. Ro: Mater. Chem. Phys. **101** (2007) 41.
38) M. Steveson, T. Bredow, and A. R. Gerson: Phys. Chem. Chem. Phys. **4** (2002) 358.
39) W. Zhang, Y. Li, S. Zhu, and F. Wang: Catal. Today **93–95** (2004) 589.